Numerical Analysis of Aerodynamic Characteristics of Iced Rotor in Forward Flight

Xi Chen* and Qijun Zhao†
Nanjing University of Aeronautics and Astronautics, 210016 Nanjing, People's Republic of China
and
George Barakos‡
University of Glasgow, G12 8QQ Glasgow, United Kingdom

Based on a 3-D rotor icing model and the CLORNS code, aerodynamic characteristics of iced rotors in forward flight are calculated and analyzed. At first, ice accretion on the UH-1H rotor in hover, and ice accretion on the SRB rotor in forward flight are calculated. The results are used to validate the employed numerical simulation method through comparisons with experimental data. Then, the degradation of the aerodynamic characteristics of the iced SRB rotor is analyzed, and the variation of the pressure coefficients on the rotor blades is discussed in detail. Finally, parameters, such as the icing time, the temperature, and the icing position, are quantified, and conclusions are obtained. The influence of the ice accretion on the sectional aerodynamic characteristics increases along the spanwise direction, and deicing near the 0.7R blade section should be preferred at the beginning of the ice accretion. Finally, it is concluded that ice will not be removed in time if the deicer is activated based solely on the variation of the rotor aerodynamics.

NOMENCLATUREH

W = vector of conservative variables

* Phd student, School of Aeronautics and Astronautics

† Professor, School of Aeronautics and Astronautics

‡ Professor, CFD Laboratory, School of Engineering

F = vector of convective fluxes

F_v = vector of viscous fluxes

h_f = thickness of the water film, m

u_f = mean velocity of the water film, m×s^{-1}

u_{ref} = absolute velocity of the unit on the blade, m×s^{-1}

A = area of the cell on the blade surface, m^2

f_{cen} = centrifugal force, kg×m×s^{-2}

dt = actual duration time of the centrifugal force working on the water film in the cell, s

l = unit vectors of the cell along different direction (I, J, K)

ρ_{ice} = density of ice， kg×m^{-3}

h_{ice} = thickness of the ice, m

m = mass in the mass balances, kg×s^{-1}

q = heat in the thermal balances, W×s^{-1}

c = chord, m

Δt = interval time in icing model, s

ΔT = interval time of coupling CFD solver with icing model, s

α = droplet volume fraction

ρ_w = density of water, kg×m^{-3}

$\vec{q}$ = absolute velocity, m×s^{-1}

$\vec{q}_\omega$ = convective velocity, m×s^{-1}

d_d = diameter of the water droplet, m

μ_a = dynamic viscosity of the air, N×s×m^{-2}

C_d = drag coefficient of the water droplet in air

Re_d = relative Reynolds number

S = possibility of that a grid cell becomes a shadow zone cell

η = convergence factor in the shadow zone model

Subscript

d = water droplet

a = airflow over the rotor

f = water film

imp = water impinged on the surface

out = water flowing out of the cell

in = water flowing into the cell from adjacent cells

so = water freezing on the surface

evp = water evaporated and sublimated in the cell

p = present cell

cri = defined value of the shadow zone cell

Abbreviation

3-D = three dimensional

2-D = two dimensional

INTRODUCTION

Ice accretion is a significant factor limiting the safe flight envelope of aircraft [1]. When helicopters fly in icing conditions, ice accretion may occur on blades of the rotor, and the aerodynamic shape of the rotor may be degraded [2, 3]. Consequently, research in the influence mechanism of the ice accretion on the aerodynamic characteristics of rotors is an important issue in helicopter safety.

At present, there are few experimental works on the aerodynamic characteristic of iced rotors in the public domain [4-7]. Korkan [4, 5] studied the aerodynamics of helicopter model rotors with attached simulated ice shapes using experiments. Lee [6] also studied iced rotors in a wind tunnel at full scale. The rotor was a replica of the main rotor of the UH-1H helicopter, hovering in an artificial cloud [7]. Theses measurement for the aerodynamic characteristics of iced rotors only approximate real ice accretion, due to the limitations of the experiments and safety considerations. With the development of computers, numerical simulation methods provide the possibility to obtain the aerodynamic characteristic variation of rotors in ice accretion.

In numerical simulation methods for iced rotors, predicting accurate ice shapes is a key problem. In recent years, many numerical codes have been successfully developed to simulate ice accretion on aircraft [8-10], for example: LEWICE, ONERA, FENSAP-ICE, POLIMICE, etc. There are also some developments in icing models and the icing prediction methods [11, 12]. However, current works mainly focus on fixed-wing aircraft. Rotors are operated in a strong non-linear vortex flowfield containing 3-D flow features, unsteady flow and centrifugal forces [13, 14]. These features were not considered in previous studies.

In addition to complex simulation methods for predicting ice accretion on rotors, some simplified methods are also developed [15-22]. Based on the Lewice3D, Narducci [15, 16] developed an analysis method to evaluate the ice accretion for a helicopter rotor. Rajmohan [17] developed a quasi-steady numerical method for ice accretion on helicopter rotors in forward flight using Lewice3D. Bain [18] used the same approach to predict ice accretion and ice shedding for rotors in forward flight. All these methods extracted representative airfoil conditions for blade sections at different radial and azimuthal locations, and predicted the ice accretion using 2-D simulations, as mentioned in reference 16. Ice accretion on rotors can be conveniently achieved using these methods, but it may be difficult to obtain accurate 3-D ice shapes. In addition, an aerodynamic method based on a simplified icing model, ignoring 3-D effects and the centrifugal force, may not yield accurate results. Based on a simple assumption that liquid water flow and mass transfer is mainly affected by the shear stress and the centrifugal force, Zhao [19] studied the ice accretion on rotor in hover considering the centrifugal force into account. Similarly, Wang [20, 21] developed an icing model accounting for the influence of centrifugal force. They both obtained some meaningful results and verified the importance of the centrifugal force in the icing process on rotors. However, the rotor icing models need to be further developed, and the researches on the mechanism of ice accretion and iced rotor aerodynamics are also need for more reliable icing simulation.

In addition, there are still other questions in the aerodynamics of iced rotors. Ice accretion is an evolutionary, complex process, affected by numerous weather and flight parameters, such as the advancing ratio, the temperature and the icing position. At present, a parametric analysis of the aerodynamic characteristics of iced rotors has not been carried out.

Based on the previous work [19, 23] with the Chinese Laboratory of Rotorcraft Navier-Stokes (CLORNS) code [24], a method for studying the influence of ice accretion on aerodynamic characteristics of rotor is developed, which

contains several improvements, such as a shadow zone dispersion model in Eulerian method and a developed 3-D icing model accounting for the velocity of the water film. The main objective of the present work is focused on developing better understanding of the mechanism of ice accretion and the effects of icing on the aerodynamics of the rotor in forward flight. The experimental data of the MS(1)-317 [25], NACA0012 [26], and NACA23012 airfoils obtained at the NASA Langley Low Turbulence Pressure Tunnel (LTPT) [27], the Helicopter Icing Flight Test (HIFT) program [28] and the Spinning Rotor Blade (SRB) developed at the Anti-icing Material International Laboratory [29] are used to validate the present numerical method. The aerodynamic characteristics of the iced SRB rotor in forward flight are calculated and analyzed, and the variation of the pressure coefficients on the rotor blade surfaces are detailed. Then, the effects of the icing parameters, such as the temperature, the icing time, and the icing position, on the aerodynamic characteristics of rotor in forward flight are calculated and analyzed systematically, and some new conclusions are drawn. The novelty of the paper is hinged upon our claim that this is one, if not the first, study of the aerodynamic characteristic of 3D iced rotor without 2D icing assumptions.

NUMERICAL METHODS

The proposed numerical simulation approach for the ice accretion on rotors consists of several modules, including the CFD solver module, the Eulerian method for obtaining the droplet impingement property on the rotor, the 3-D rotor icing model and the grid regeneration for the iced rotor. The procedure of ice accretion on a rotor is illustrated in Figure 1.

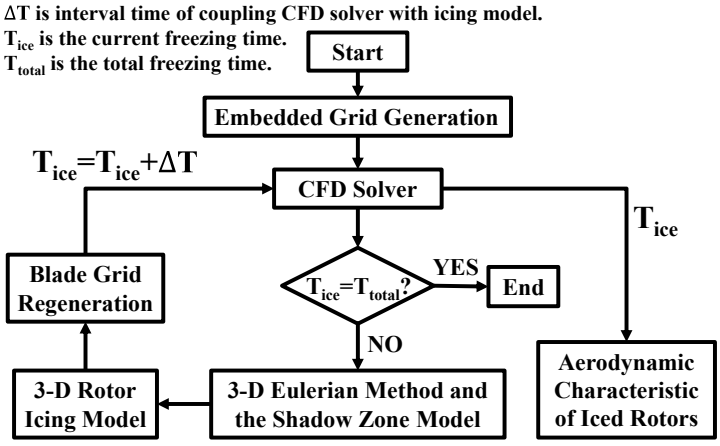

Figure 1. Overview of the numerical simulation process for ice accretion on rotor.

The Chinese Laboratory of Rotorcraft Navier-Stokes (CLORNS) code is employed to predict the complex unsteady rotor flowfield [24]. Grids around the rotor blade are generated by interpolating and folding airfoil grids

constructed by solving Poisson's equation. Structured Cartesian grids are used as the background grid of a chimera system. The governing equations in integral form for predicting the flowfield of the rotor are described as:

$$\frac{\partial}{\partial t}\iiint \vec{W} d\Omega + \iint_S (\vec{F} - \vec{F}_v)\cdot \vec{n} ds = 0 \tag{1}$$

In CLORNS, a disturbance diffraction method for hole-cell identification and a minimum distance scheme for donor cell searches are used with high efficiency and universality. The explicit Runge-Kutta and implicit Lower-Upper Symmetric Gauss-Seidel (LU-SGS) methods are both available for solving the unsteady Reynolds-averaged Navier-Stokes equations. Three alternative spatial discretization schemes are applied in the code, including a second-order central difference scheme, a third-order Roe-MUSCL scheme, and a fifth-order WENO-Roe scheme.

Based on the rotor flowfield obtained by CLORNS, the Eulerian method is applied for the simulation of the water droplet field around the rotor. The continuity and momentum equations for droplets around a rotor in 3-D could be simplified as:

$$\frac{\partial}{\partial t}\iiint_\Omega \vec{W}_d d\Omega + \iint_S \vec{F}_d \cdot \vec{n} ds = \iiint_\Omega \vec{R} + \vec{R}_d d\Omega \tag{2}$$

$$\vec{W}_d = \begin{Bmatrix} \rho_d \alpha \\ \rho_d \alpha u_d \\ \rho_d \alpha v_d \\ \rho_d \alpha w_d \end{Bmatrix}, \vec{F}_d = \begin{Bmatrix} \rho_d \alpha (\vec{q}_d - \vec{q}_\omega) \\ \rho_d \alpha u_d (\vec{q}_d - \vec{q}_\omega) \\ \rho_d \alpha v_d (\vec{q}_d - \vec{q}_\omega) \\ \rho_d \alpha w_d (\vec{q}_d - \vec{q}_\omega) \end{Bmatrix}, \vec{R}_d = \begin{bmatrix} 0 \\ \rho_d \alpha K(u_a - u_d) \\ \rho_d \alpha K(v_a - v_d) + \rho_d \alpha g \\ \rho_d \alpha K(w_a - w_d) \end{bmatrix} \tag{3}$$

where, K is given as:

$$K = \frac{0.75 \cdot \mu_a \cdot C_D \,\mathrm{Re}_d}{\rho_w d_d^2} \tag{4}$$

The expression $C_d \,\mathrm{Re}_d$ and Re_d is given as:

$$C_d \,\mathrm{Re}_d = \begin{cases} 24 \cdot (1 + 0.15\,\mathrm{Re}_d^{\,0.687}), \mathrm{Re}_d \le 1000 \\ 0.44 \cdot \mathrm{Re}_d \qquad\qquad\quad , \mathrm{Re}_d > 1000 \end{cases}, \quad \mathrm{Re}_d = \frac{\rho_a |\vec{q}_a - \vec{q}_d| d_d}{\mu_a} \tag{5}$$

In the process of supercool droplets movement, there is always a region where no droplets pass through, due to the presence of the blade in their motion path. This region is called the shadow zone or the shadow region, and the apparent

density (α) in the Eulerian method is very low. Based on this, a shadow zone dispersion model is presented. In this model, the formation of the shadow zone is accelerated to avoid numerical problems, such as loss of stability of the code and density impulses [30].

The variable *S*, is related to the variation of α , and denotes the possibility of that a grid cell becoming a shadow zone cell. This is updated with each iteration step. If a cell is marked as a shadow zone cell, the cell is removed from the computational domain. Figure 2 shows a flowchart of the calculation of the variable *S* during an iteration step.

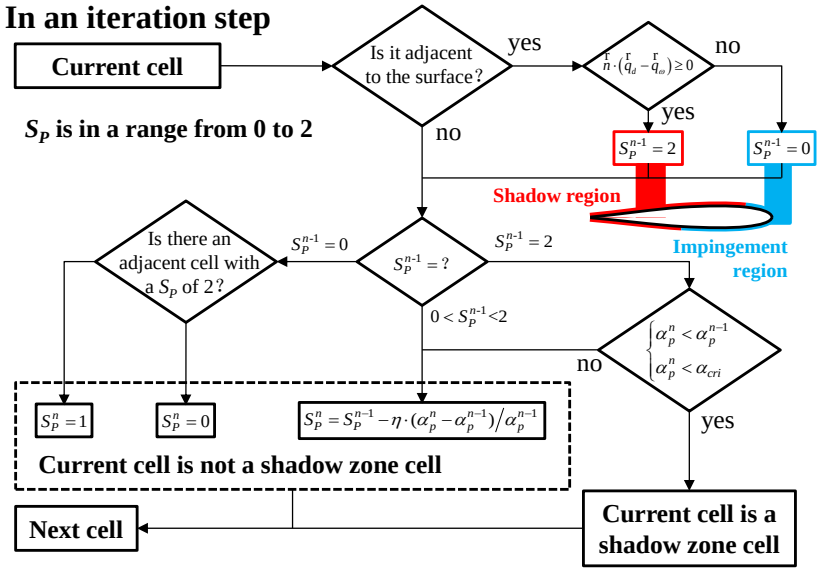

Figure 2. Flowchart of the calculation of the variable S.

Since there are some differences between the ice accretion on the rotor and on the fixed wing [31], the 3-D rotor icing model considering the centrifugal force and the water film movement is applied to predict ice accretion. In this model, water droplets impinging on a unit area turn into a thin, continuous film of water covering the blade and iced surfaces. The velocity of the water film is determined by the airflow and the centrifugal force due to the rotor rotation. Figure 3 shows the water film movement in a cell on the blade surface, according to the employed model.

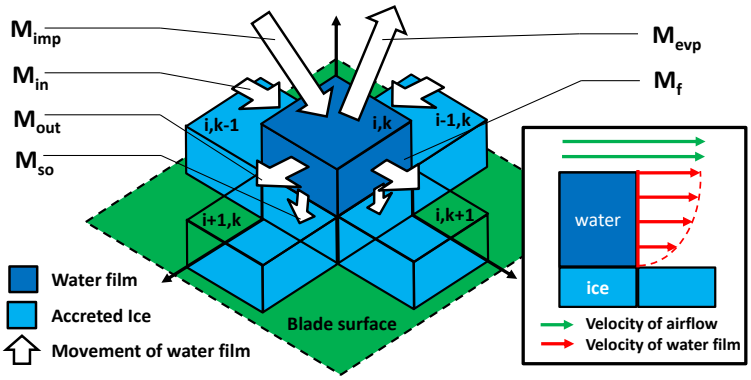

Figure 3. Water film movement on the surface of the blade.

In the rotor icing model, the mass and thermal balances are performed for each control cell:

$$m_{imp} + m_f(t) + \sum m_{in} = m_f(t+\Delta t) + m_{so} + \sum m_{out} + m_{evp} \tag{6}$$

$$q_{imp} + q_f(t) + \sum q_{in} = q_{evp} + q_{so} + \sum q_{out} + q_{hc} + q_{cnd} + q_f(t+\Delta t) \tag{7}$$

where, *imp* stands for impingement, *evp* for evaporation and sublimation , *so* for solidification, *f* for the water film, *in* and *out* stand for the movement of water film, *hc* for convection heat transfer, and *cnd* for the heat from the deicer.

Introducing the freezing fraction F, it is calculated by solving the mass and thermal balance equations, which assumes a freezing temperature. Then, the water freezing on the surface and the height of the water film are defined as:

$$m_{so} = F \times \left[m_f(t) + m_{imp} + \sum m_{in} - m_{evp} \right] \tag{8}$$

$$h_f = \left[m_{imp} + m_f(t) + \sum m_{in} \right] / A_{unit} \tag{9}$$

$$m_{imp} = LWC \cdot A_{unit} \cdot \beta \cdot u_{ref} \tag{10}$$

The typical thickness scale of a water film on the aircraft is 1×10^{-4}m, and a linear velocity distribution normal to the film is assumed [32]. In addition, conclusions of previous investigations indicate that the centrifugal force also affects the water film movement, displacing it towards the blade tip [19, 23]. The mean velocity of the water film on the blade surface and m_{out} can be expressed as:

$$\vec{u}_f = \nabla p \cdot \frac{h_f^2}{3\mu_w} + \frac{\vec{\tau} h_f}{2\mu_w} + \frac{\vec{f}_{cen}}{m_f(t)} \times dt, \quad \sum m_{out} = \left|\vec{u}_f\right| \cdot h_f \tag{11}$$

With the ice amount (m_{so}) is determined, the ice volume and thickness are calculated using:

$$V_{ice} = m_{so} / \rho_{ice}, \quad h_{ice} = V_{ice} / A \tag{12}$$

CFD grid nodes on the iced surface must be moved due to the ice accretion. Assuming that the ice grows in the normal direction to the surface, the displacement of each node on the iced front is h_{ice}.

CALCULATED RESULTS AND ANALYSES

A. Aerodynamic characteristics on clean and iced NACA23012 airfoil

The experimental data for an iced NACA23012 airfoil, obtained at the NASA Langley Low Turbulence Pressure Tunnel (LTPT) was selected to validate the accuracy of the employed numerical method. The LTPT measurements were at Mach number of 0.208 and at Reynolds number of approximately 2×10^6 [27]. Figure 4 shows the modified NACA23012 airfoil and the grids used in the present study.

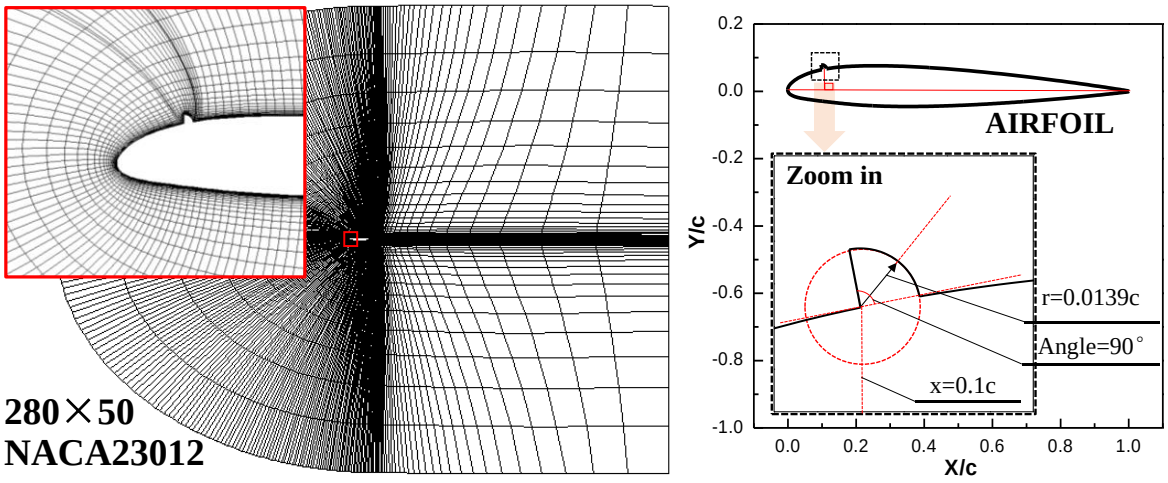

Figure 4. The modified NACA23012 airfoil and the grids around the airfoil.

Figure 5 shows the aerodynamic characteristics of the modified obtained from different turbulence models. As seen, the results are all close to the experiment data, and the k-ω turbulence model is ever so slightly closer to the test. With this in mind, the k-ω turbulence model is used in the subsequent calculations.

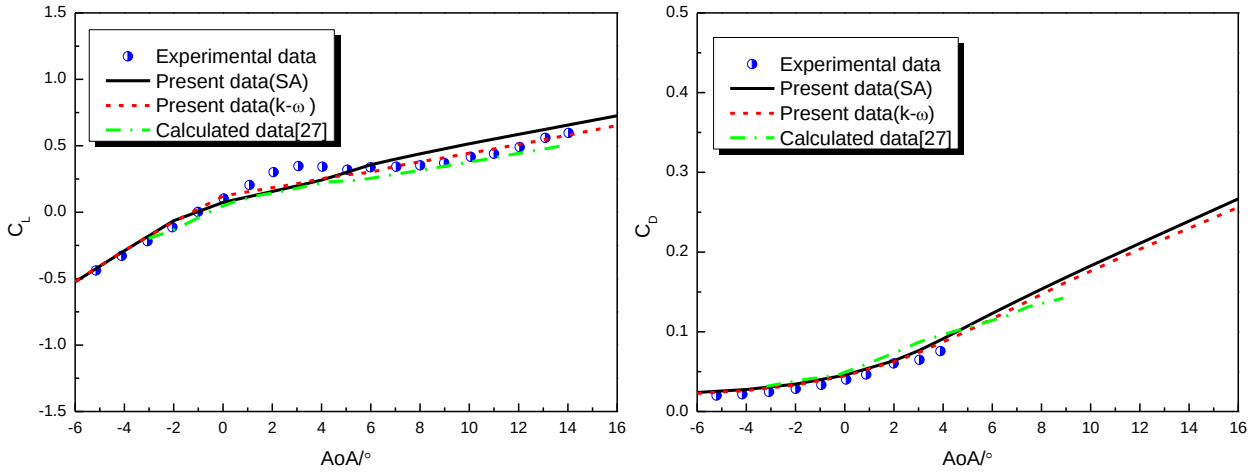

(a) C_L **(b) C_D**

Figure 5. The NACA23012 airfoil and the grids around the airfoil.

B. Validation of aerodynamic characteristics on the clean rotor

The flight tests for AH-1G performed at the NASA Ames Research Center were selected for validation. The rotor was two-bladed, of rectangular-platform, and teetering. The blade had a linear twist of -10° from blade root to blade tip, and the blade aspect ratio was 9.8. The experiment were made at an advance ratio of 0.19 and a tip Mach number of 0.65 [33].

Figure 6 shows pressure coefficient distributions at 0.6R and at different blade azimuths. Figure 7 shows the sectional normal force of different blade sections. From the figures, it can be seen that the agreement between calculated results and experimental data is good, indicating that the present CFD method is able to approximate the aerodynamic characteristic of the clean rotor in forward flight.

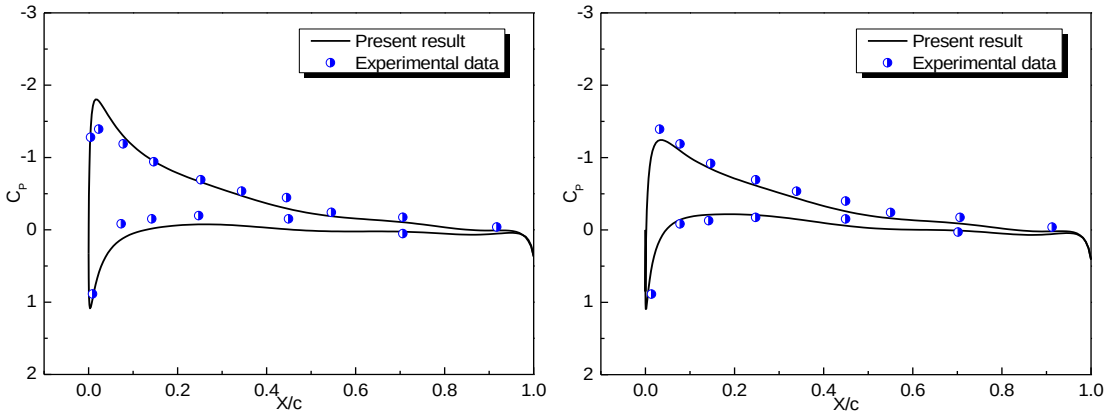

(a) 0.6R, 30° azimuth angle **(b) 0.6R, 90° azimuth angle**

Figure 6. Pressure coefficient distributions of different blade sections in forward flight.

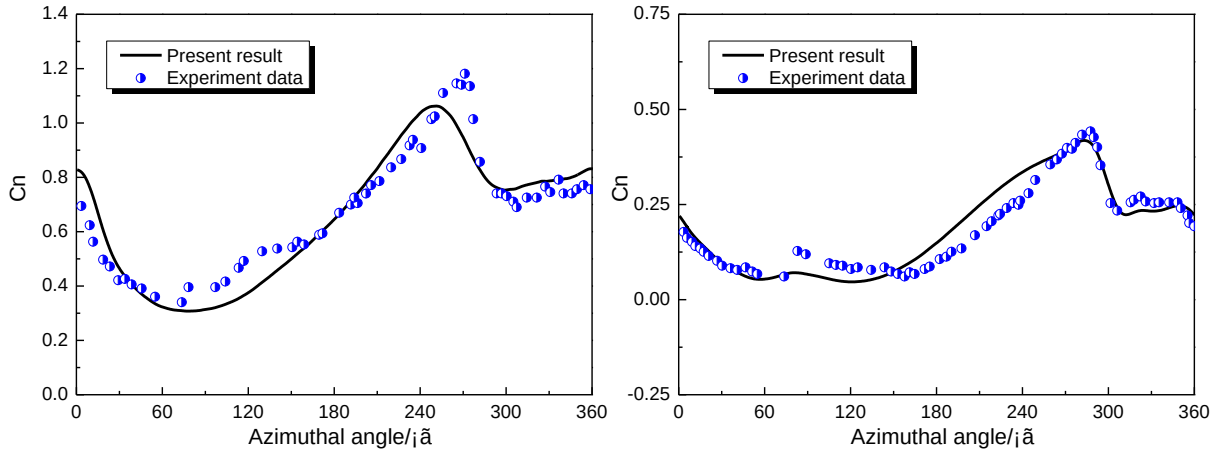

(a) r= 0.6R **(b)r= 0.9R**

Figure 7. Sectional normal force coefficient of different blade sections in forward flight.

C. Validation of droplet impingement property and ice shape on airfoil

The experimental data of droplets impingement on the MS(1)-317 airfoil [25] was selected to validate the accuracy of the employed numerical method for the droplet impingement property. The airfoil chord was 0.9114m, and the inflow velocity was 105.4m/s. The median volumetric drop diameter was 11μm, and the angle of attack was 0º and 8º. Figure 8 shows the comparison of the droplet impingement property on the airfoil between the calculated results and experimental data. As seen, the result obtained from the present method are close to the experiment data, indicating that the present method is able to obtain a reliable droplets impingement property.

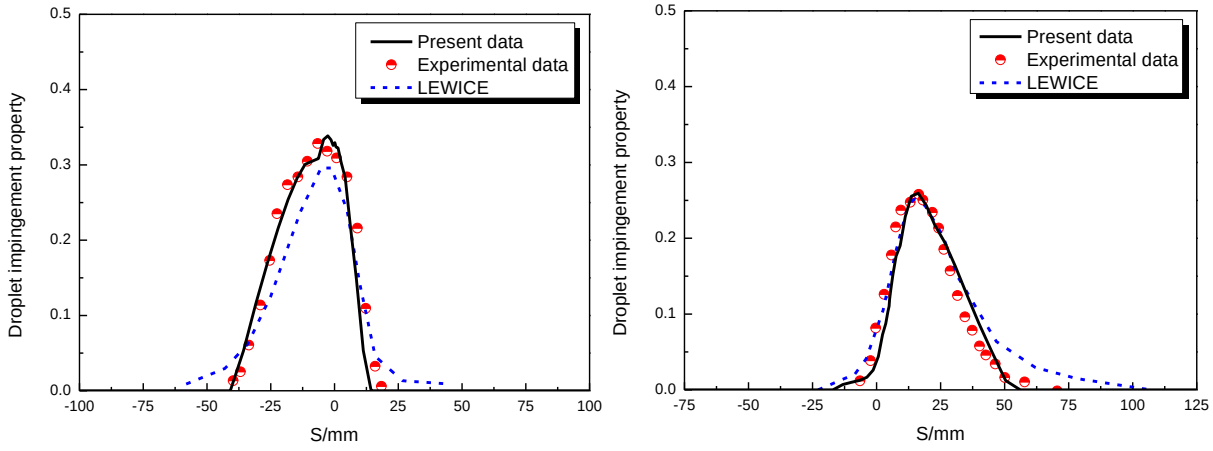

(a)AOA= 0º **(b)AOA= 8º**

Figure 8. Comparison of the droplet impingement property on the airfoil

The experimental ice accretion shapes on the NACA0012 airfoil [26] were selected to validate the accuracy of the employed numerical method for the ice accretion. The chord was 0.5334m, and the inflow velocity was 67.05m/s. The median volumetric drop diameter was 20 μm, and the liquid water content was 1 g/m^3. The total accretion time was 7 minutes. Four different time intervals (420s, 105s, 70s and 35s) were selected to analysis the influence of the time step on the ice amount respectively.

Figure 9 shows the comparison of the ice shapes on the airfoil between the calculated results and experiment data at different time intervals. As seen, the calculated results are all close to the experiment data, and the influence of the time step on the ice shape is decreasing with the reduction of ΔT. Additionally, the difference of the ice shape between the calculated result and experiments is bigger when ΔT is small (ΔT=35s). As a result, a moderate ΔT (one third of the total icing time) was selected in the subsequent calculations.

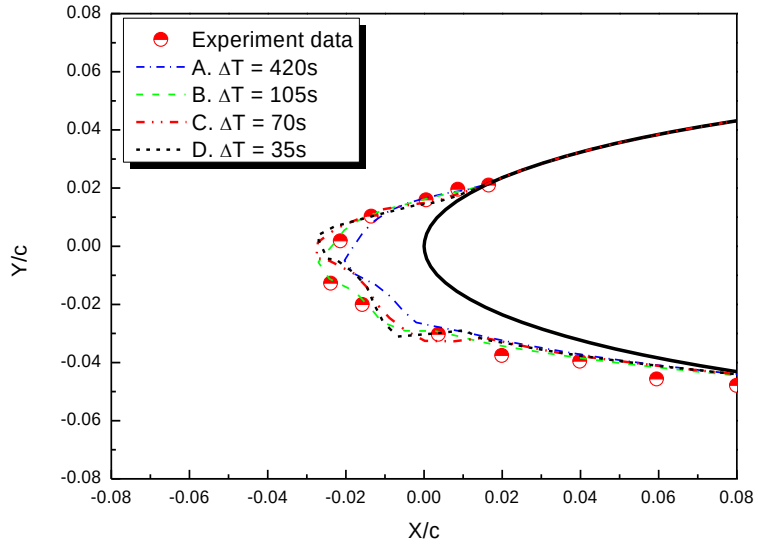

Figure 9. Comparison of the ice shape on the airfoil with different time steps

D. Validation of numerical simulation of ice accretion on rotors

The Helicopter Icing Flight Test (HIFT) program [28] was selected for validation. The rotor of the Bell UH-1H helicopter had a conventional NACA 0012 airfoil with a constant chord of 0.5334m. The blade radius was 7.3152m, and the rotor blade had a linear 10.9° negative twist along the radius. The rotational speed of the main rotor was 33.9 rad/s, and the blade-tip Mach number was 0.79. During the flight tests, the temperature was -19°C, and the total

accretion time was 3 minutes. The median volumetric drop diameter (MVD) was 30 μm, and the liquid water content (LWC) was 0.7 g/m^3.

Considering that ice accretion mainly occurs on the leading-edge of the blade, several different blade grids were used in this case. Their difference was the grid refinement near the leading-edge of the blade, as shown in Figure 10. Blade A (the coarse grids) had a resolution of 189×49×131, and there were 129 points on the surface of each blade section. Blade B (the Medium grids) had a resolution of 263×49×131, and there were 203 points on the surface of each blade section. Blade C (the refined grids) had a resolution of 341×49×131, and there were 281 points on the surface of each blade section. For studying the influence of the nodes in the J and K directions, Blade D had a resolution of 263×39×131, Blade E had a resolution of 263×59×131, Blade F had a resolution of 263×49×101, and Blade E had a resolution of 263×49×161. The background grids had a resolution 201×99×181.

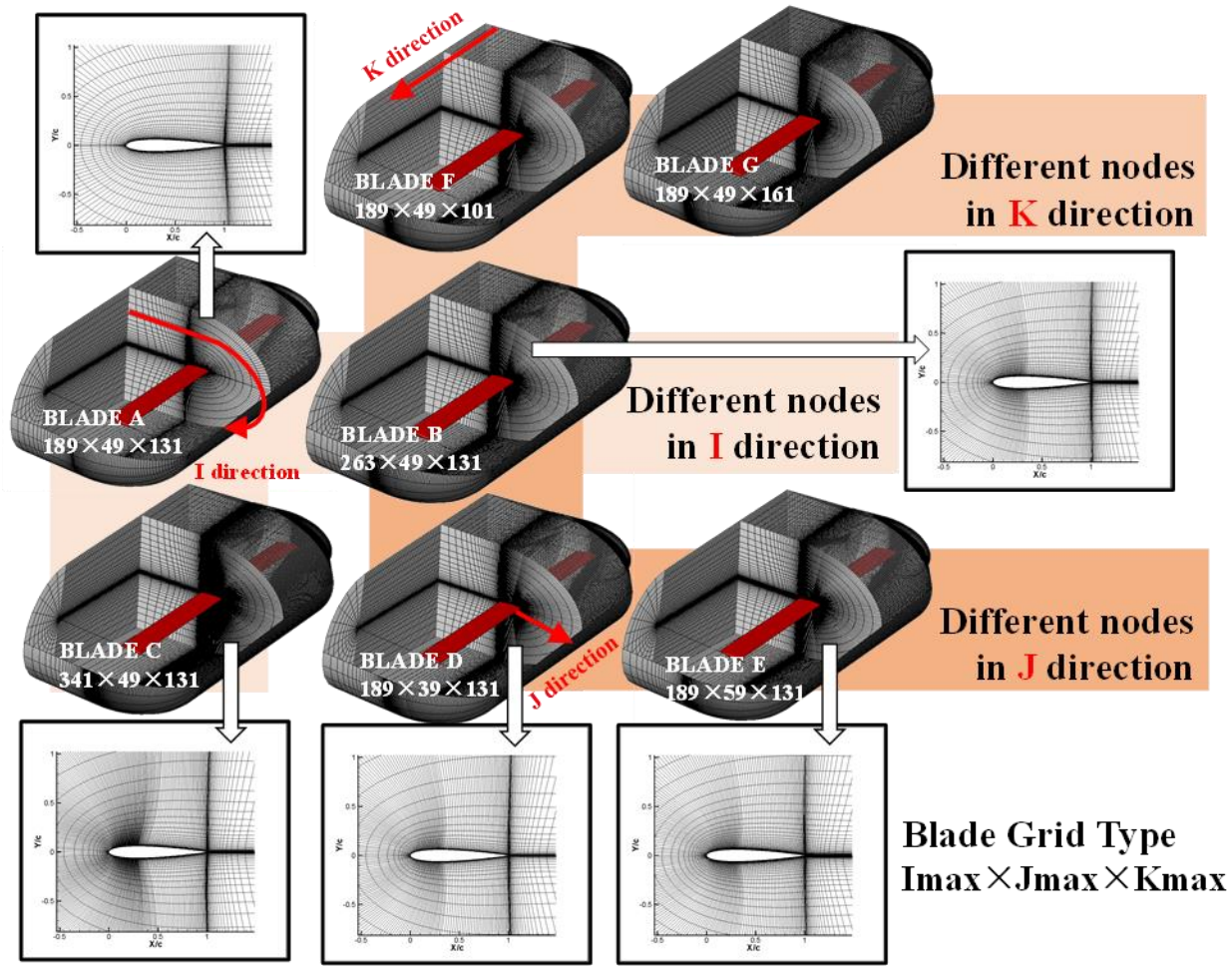

Figure 10. Seven types of the blade grids

Figure 11 shows the ice shapes at r=0.45R obtained for the different blade grids. As seen, the results obtained from the medium and refined blade grids (Blade B, C, E, F and G) are nearly the same, and the results obtained from the coarse ones (Blade A and D) lose some information near the ice horn and the ice fringe. After a systematic consideration of the computational accuracy and time, the medium grids (Blade B) was used in the subsequent calculations.

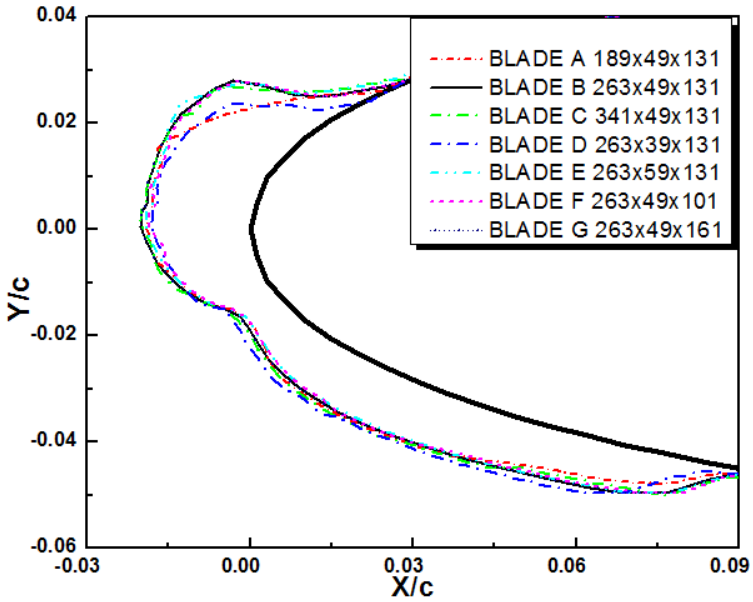

Figure 11. Sectional ice shapes obtained from different types of blade grids.

Figure 12 shows the sectional ice shapes at r=0.45R and r=0.7R and the sectional maximum ice depth variation in the spanwise direction from blade root to blade tip. In the figures, the agreement between computations and experiments is good, and is better than published results in reference 15.

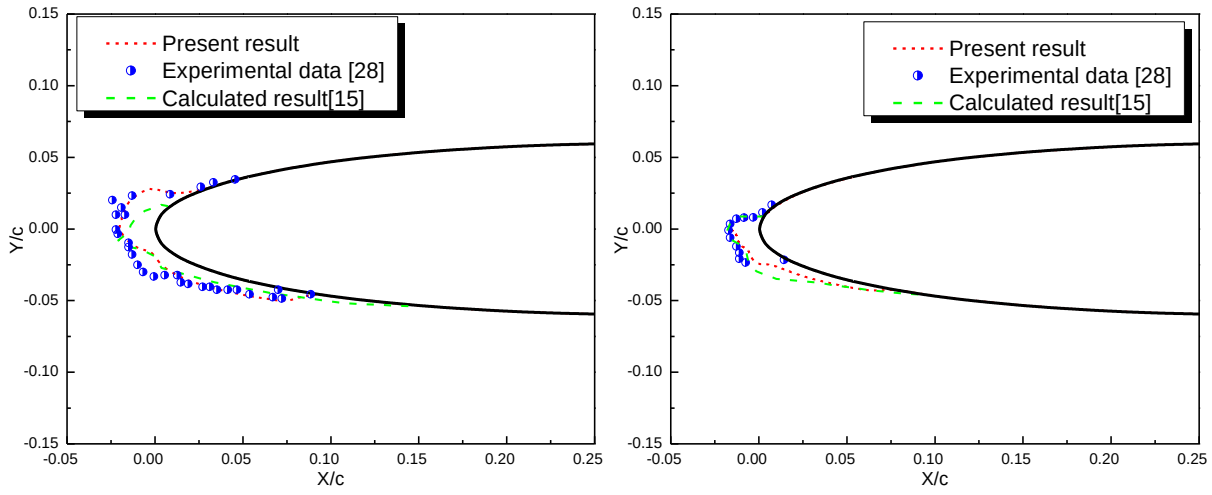

(a) r=0.45R **(b) r=0.7R**

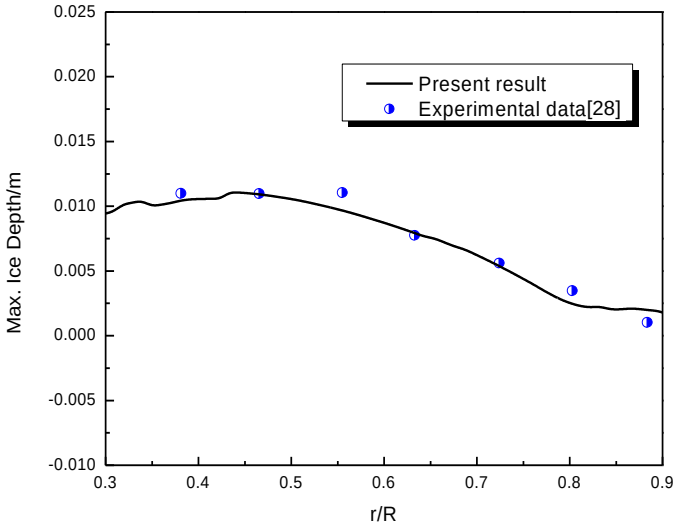

(c) Maximum ice depth of the blade in the spanwise direction.

Figure. 12 The result of ice accretion on the UH-1H rotor in hover.

The experimental data of the Spinning Rotor Blade (SRB) developed at the Anti-icing Material International Laboratory [29] was selected to validate the accuracy of the numerical method for ice accretion on rotors in forward flight. The rotor was a 1/18-scale model of a small helicopter. The blades were untwisted, and made of NACA 0012 sections with a constant chord 0.07 m and a root cut out of 0.075 m. The rotor diameter was 0.78 m. The forward flight speed of the rotor was 15 m/s and the blade-tip speed was 130 m/s, giving an advance ration of 0.115. For the experiments, the LWC was 0.84 g/m^3, and the MVD was 27 μm. The ambient temperature was -15℃. In addition, the rotor operated at a fixed collective of 6° with zero cyclic.

Figure 13 shows sectional ice shapes, and ice thickness at the blade tip. In the figure, the ice amount calculated by the proposed method is close to the experimental data, and it is better than results with the empirical formula of reference 29 and published results of reference 18.

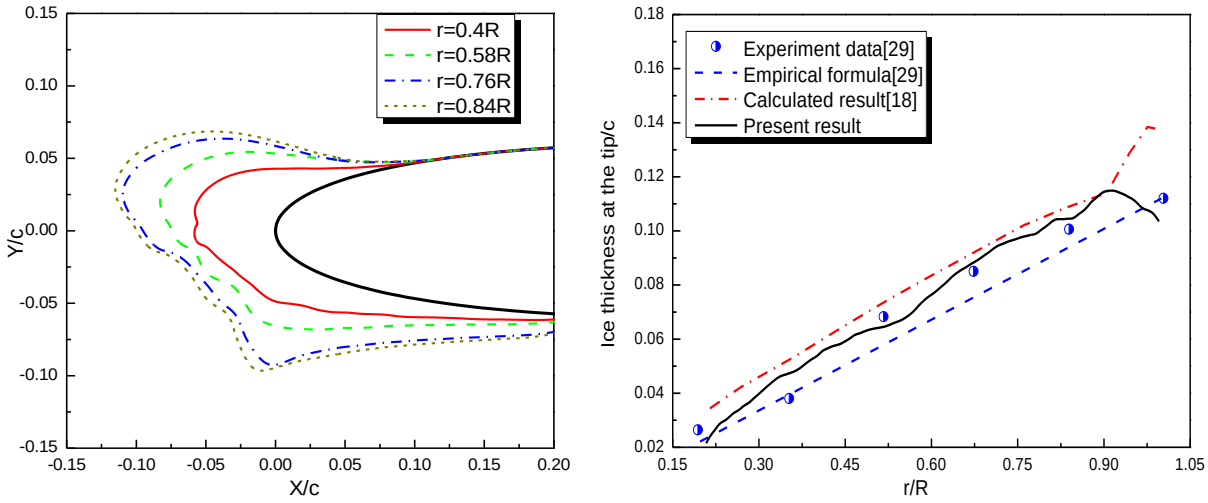

(a) Sectional ice shapes **(b) Ice thickness at the tip**

Figure 13. The result of ice accretion on the SRB rotor in forward flight.

In references 15 and 18, the traditional numerical methods for ice accretion on rotor were used. In these methods, representative airfoil conditions for blade sections at different radial and azimuthal locations were extracted, and the ice accretion was predicted by using 2-D simulations. Through the comparison of calculated results of the ice accretion on rotors, the proposed numerical simulation method with a 3-D icing model can provide a more reliable ice shape for analyzing the influence of the ice accretion on aerodynamic characteristics of rotors.

E. Influence of ice on aerodynamic characteristics of the rotor in forward flight

The iced SRB rotor at the conditions mentioned above was selected to analyze the influence of ice accretion on the aerodynamic characteristics of rotors. According to the experimental parameters in the ice accretion process [29], the rotor operated at a fixed collective of 6° with zero cyclic. Figure 14(a) shows the comparison of lift coefficient (C_L) between the clean and iced rotors. In the advancing blade, the lift coefficient changes between 0° and 120° azimuth angles, and it decreases by a maximum of 18% near 60° of azimuth. On the retreating side, the lift coefficient changes between 250° and 330°, and decreases by a maximum of 9% near 300° of azimuth. Figure 14(b) shows the comparison of the torque coefficient (C_Q) between the clean and iced SRB rotors. There is an obvious increase when ice forms on the blade surface.

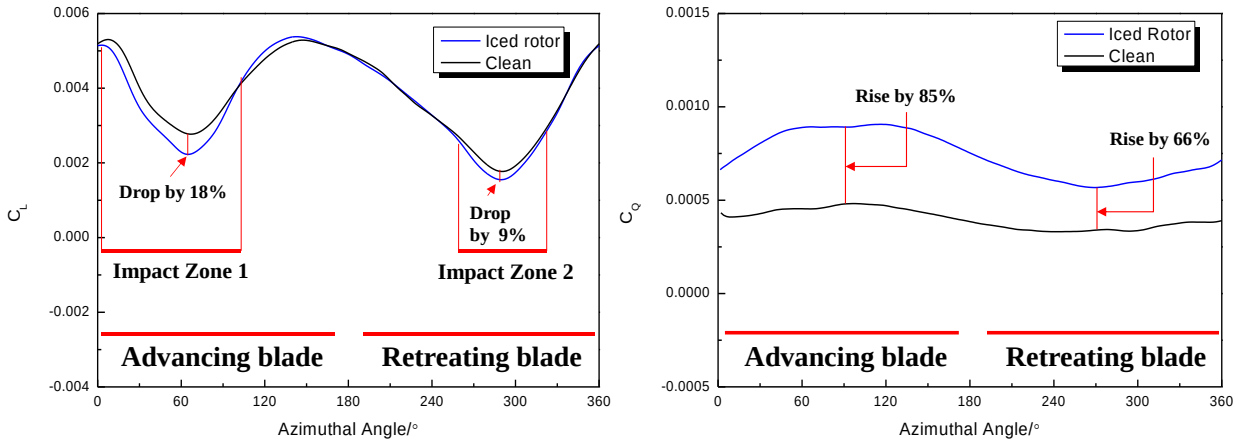

(a) Lift coefficient **(b) Torque coefficient**

Figure 14. Distributions of the lift coefficient and torque coefficient of clean and iced SRB rotors.

Figure 15 shows the pressure distributions on the blade surface along the azimuth. As seen, the change in pressure distribution due to the ice accretion increases along the spanwise direction from the blade root to the blade tip, and the variation of the pressure on the lower surface is much bigger than that on the upper surface. Due to ice near the leading edge of the blade, there is a significant change in the movement of the airflow over the blade surface, resulting in a low pressure area emerging on the lower surface compared with the clean one. Overall, the low pressure area on the lower surface extends from the middle of the blade to the blade tip, and is close to the leading edge of the blade.

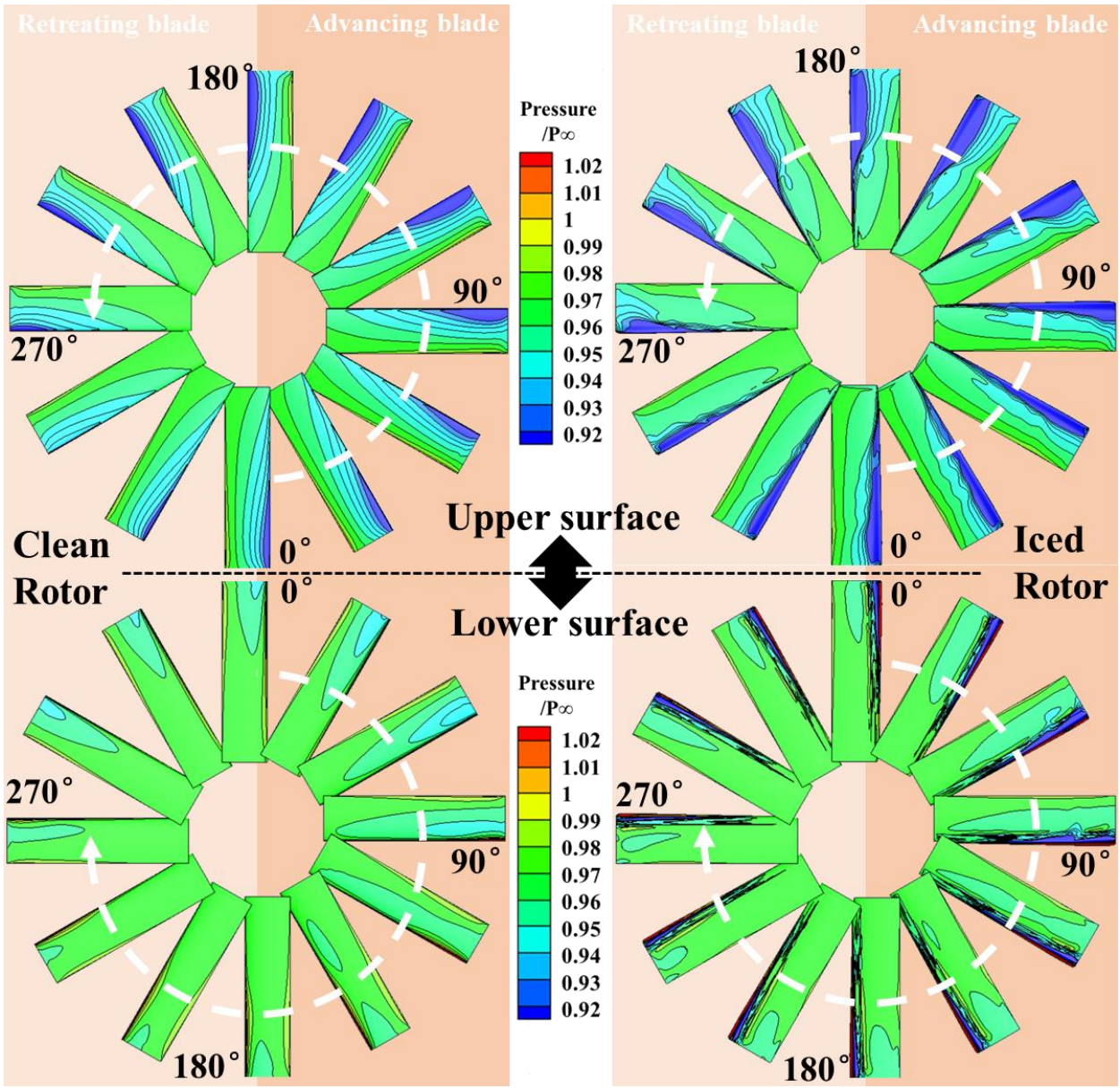

Figure 15. Pressure distributions on the blade surface at different azimuth angles with and without ice.

Considering the decrease of lift coefficient at 60° of azimuth is the most significant on the advancing side, Figure 16 shows the sectional pressure distribution of the blade at 60° of azimuth with and without ice. At 0.45R, there is no significant variation in the pressure distribution. The ice amount is small, and the iced section is of a streamlined shape as shown in Figure 16(a). At 0.85R, the ice amount is larger, and there is an obvious horn-shaped piece of ice at the leading edge of the blade. The movement of the air flow is affected by it, and a low pressure area emerges on the lower surface of the blade, where flow separation is also observed. Similarly, Figure 17 shows the sectional pressure distribution of the blade at 300° of azimuth with and without ice. Since the rotor operated at a fixed collective of 6°

with zero cyclic in this case, the main difference is the relative velocity of the blade at different azimuth angles. At 300° of azimuth, the relative velocity is smaller, and low pressure area due to the horn-shaped piece of ice is smaller.

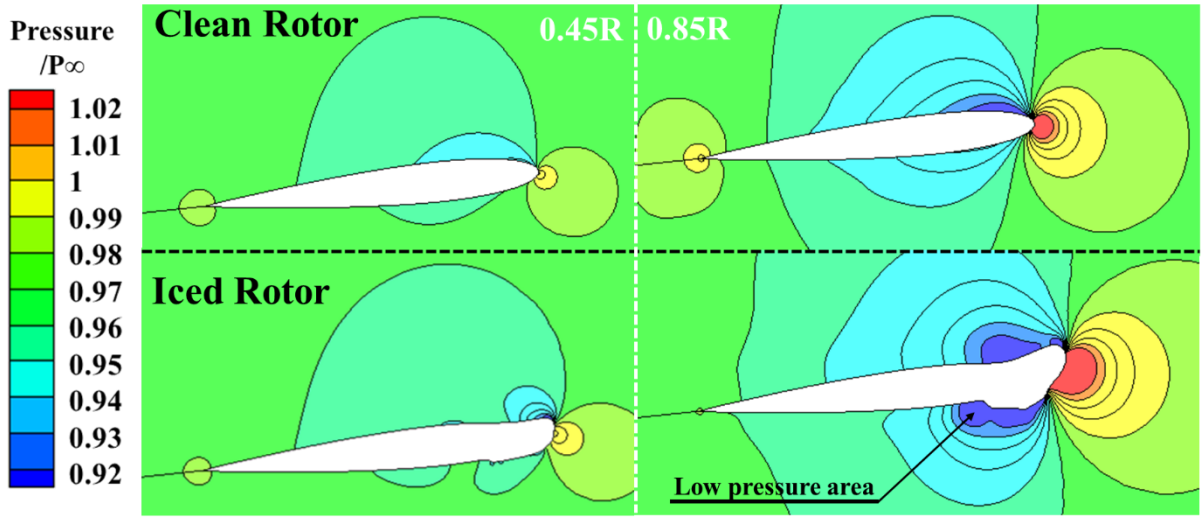

(a) 0.45R section **(b) 0.85R section**

Figure 16. Sectional pressure distribution of clean and iced blade at 60° azimuth angle.

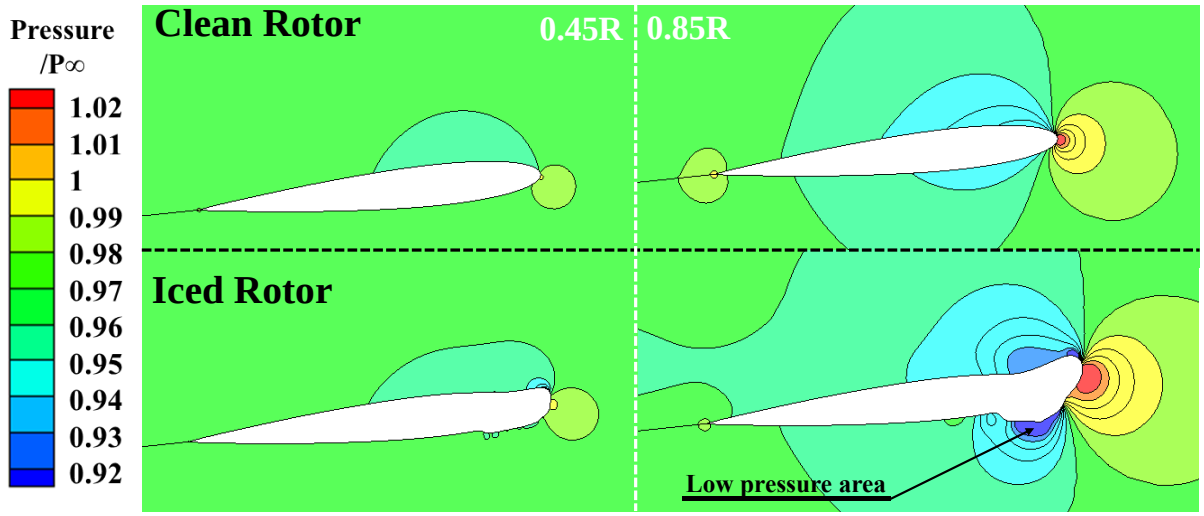

(a) 0.45R section **(b) 0.85R section**

Figure 17. Sectional pressure distribution of clean and iced blade at 300° azimuth angle.

Additionally, Figure 18 shows the 0.45R sectional pressure coefficient distribution at two azimuth angles. Compared with the clean rotor, the pressure coefficient decreases on the lower surface and increases on the upper surface, causing the loss of sectional lift. However, the lift force is likely to increase, since the chord is longer by the accreted ice at the leading edge of the blade. As a result, there may not be a significant variation in the sectional lift force near the blade root, and there may even be a small increase of the lift force at certain conditions.

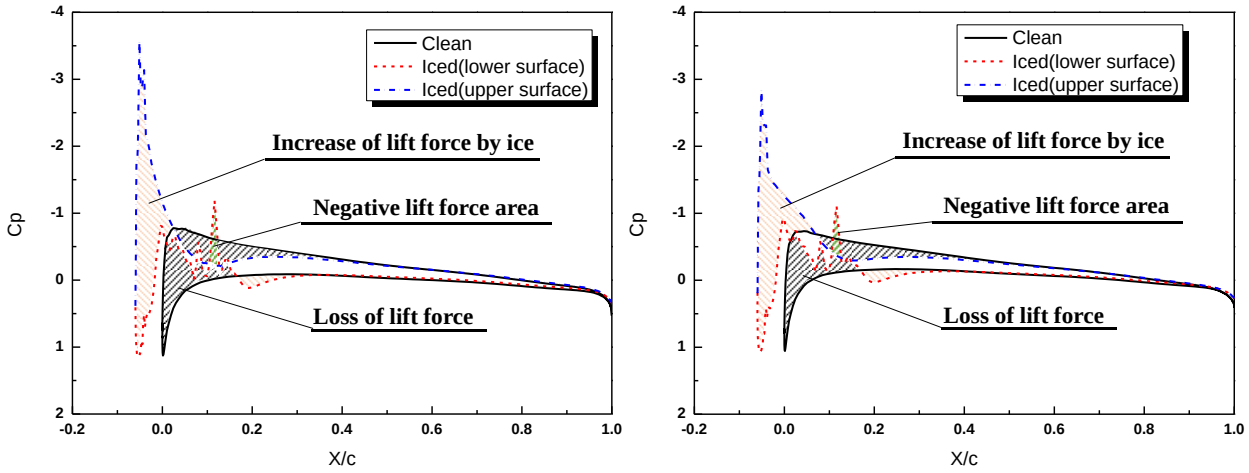

(a) 60° azimuth angle **(b) 300° azimuth angle**

Figure 18. Sectional pressure coefficient distribution of clean and iced blade at r=0.45R section.

Figure 19 shows the 0.85R sectional pressure coefficient distribution at two azimuth angles. Compared with the clean rotor, the pressure coefficient markedly decreases on the lower surface and increases on the upper. This variation of the pressure coefficient not only causes lift reduction, but may even lead to the formation of a negative lift force area. Since the sectional chord is longer, the ice accretion may provide the blade with additional lift, similar to the section near the blade root. This effect is, however, smaller compared to the negative lift force and the loss of lift force, as shown in the figure. As a result, the reduction of lift force near the blade tip is stronger than that that near the blade root.

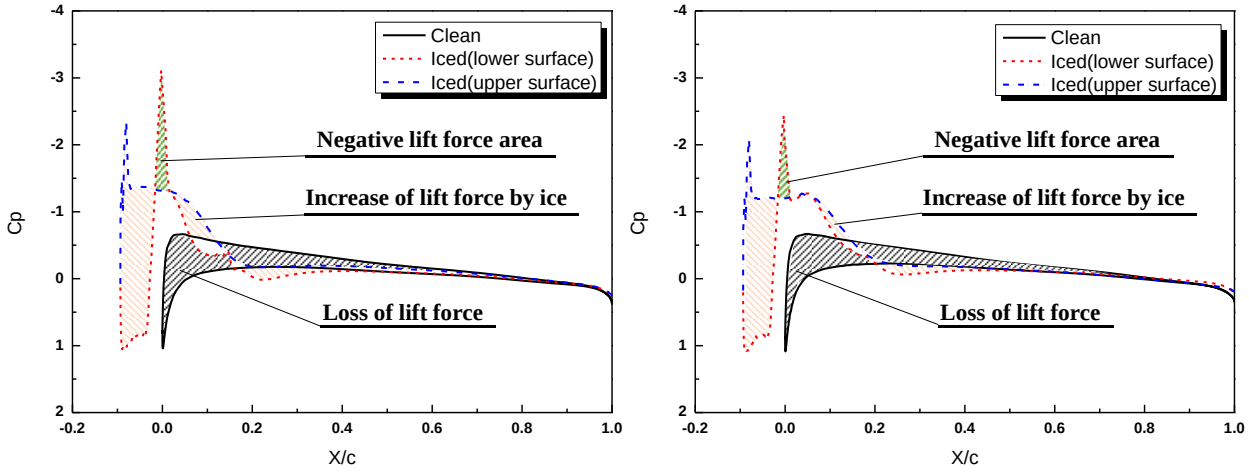

(a) 60° azimuth angle **(b) 300° azimuth angle**

Figure 19. Sectional pressure coefficient distribution of clean and iced blade at r=0.85R section.

Figure 20 shows the variation of the aerodynamic characteristics of the SRB rotor due to icing. With increased accretion time, the ice amount increases. Then, the lift coefficient decreases, and the torque coefficient increases. However, at the beginning of the ice accretion (t<40s), the increase of the torque coefficient is minor. So, if the deicer is activated only based on the variation of the torque coefficient, the ice on the blade will not be removed in time.

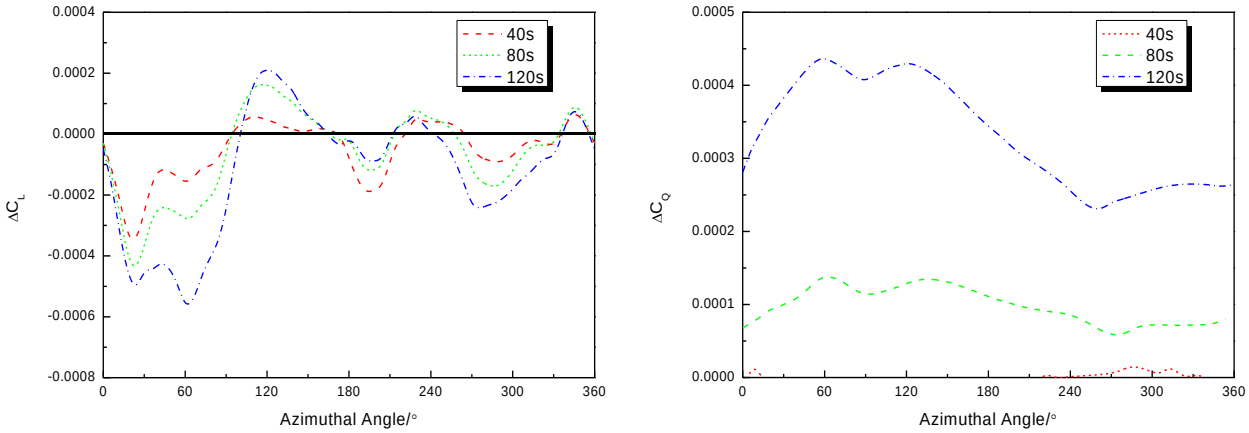

(a) Difference of the lift coefficient **(b) Difference of the torque coefficient**

Figure 20. Difference of Aerodynamic characteristics of the iced rotor in the icing process.

F. Influence of the temperature on aerodynamic characteristics of the rotor in forward flight

For studying the influence of the temperature on the aerodynamic characteristics of rotors in icing condition, the ice accretions on the SRB rotor at different temperatures were calculated. The other calculation parameters were the same as for the SRB rotor test. Figure 21 shows the sectional area of ice along the radial direction at different temperatures in forward flight. As can be seen, the sectional iced area gradually increases as temperature decreases.

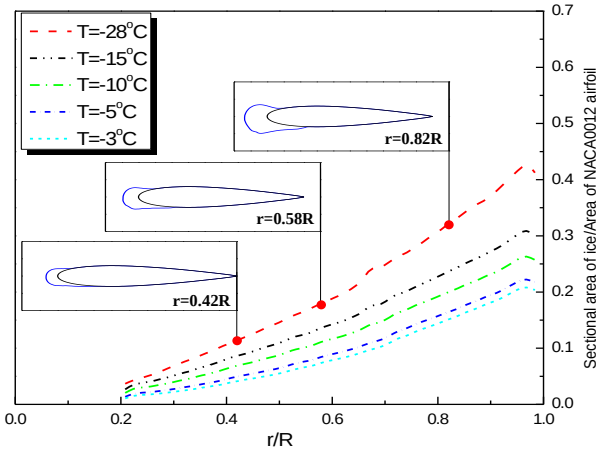

Figure 21. Ice area on different blade sections in forward flight at different temperatures.

Figure 22 shows the distributions of the lift (C_L) and torque coefficients (C_Q) of the blade at the different temperatures. In the advancing blade (near 60° azimuth), the ice formed on the blade at T=-10°C has the biggest effects on the lift force. At higher temperature (T=-5°C), the ice amount is smaller, and the lift force of the blade is not seriously affected. Although the ice amount at the lower temperature (T=-28°C) is much bigger, the lift reduction is not greatly affected. This is because that the rime ice at lower temperature has a streamline shape. Regarding the torque coefficient, there is a smaller increase at lower temperature and a larger increase at higher temperature.

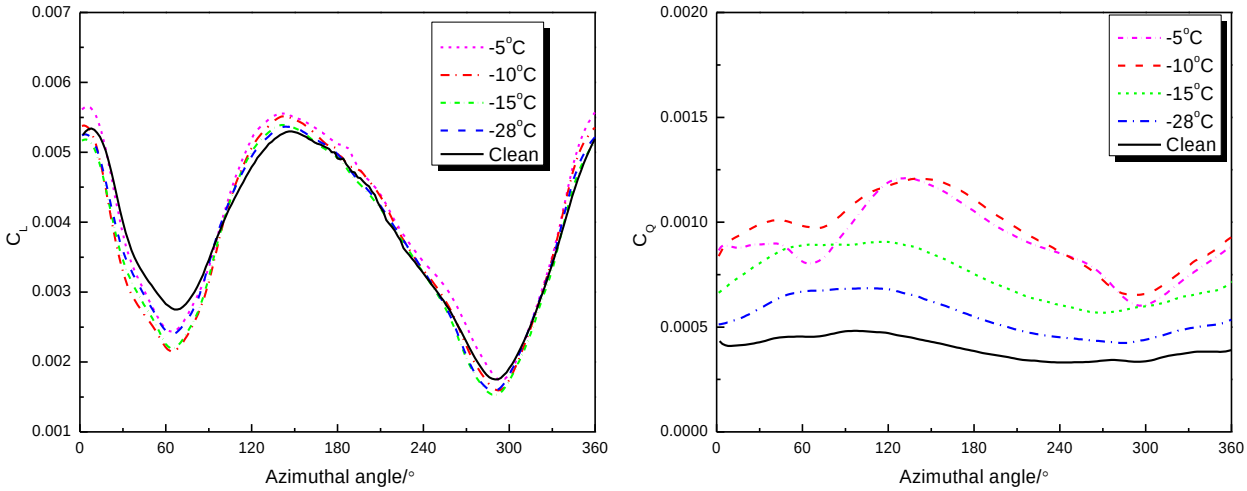

(a) Lift coefficient **(b) Torque coefficient**

Figure 22. Distributions of the lift coefficient and torque coefficient of the blade at different temperatures.

Figure 23 shows the distributions of the sectional pressure coefficient (C_P) at -5°C and -28°C temperatures. At the higher temperature (T=-10°C), the pressure coefficient on the lower surface markedly decreases, and it is smaller than that of the upper surface from 0.0c to 0.1c along the chordwise direction. Therefore, there is a larger zone of negative lift force, especially near the blade tip, and this is the main reason for the lift reduction. Also, this phenomenon is not obvious near the blade root, since ice amount is smaller. At the lower temperature (T=-28°C), the pressure coefficient on the lower surface also decreases, but the area of the negative lift force is smaller compared with that at the highest temperature.

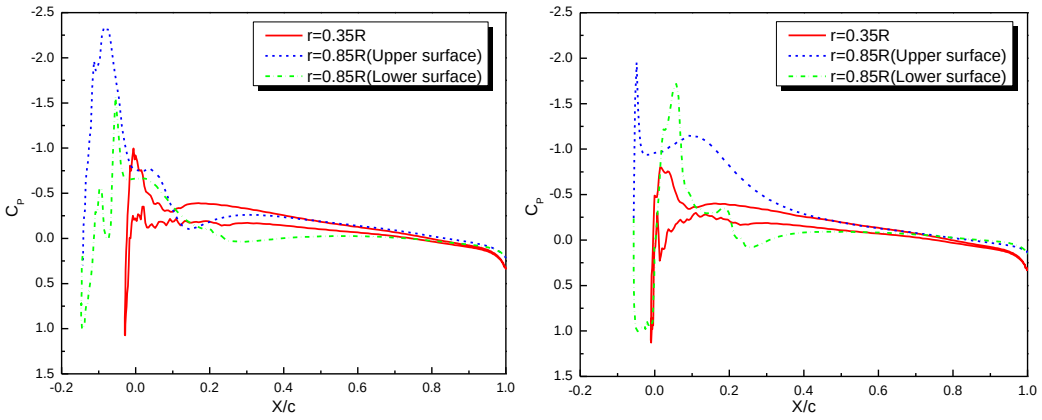

(a) T=-28°C **(b) T=-10°C**

Figure 23. Distributions of the sectional pressure coefficient at different temperatures.

G. Influence of icing position on aerodynamic characteristics of the rotor in forward flight.

At some icing conditions, there is always a small amount of ice on rotors before the rotor deicer starts. These ice shapes, albeit very small, will still have an effect on the aerodynamic characteristics of rotors.

The SRB rotor was again selected as the clean, baseline, case. Figure 24 shows one of iced rotors and the sectional ice shape. There are 9 different iced rotors, and the icing extends from 0.29R to 0.93R at intervals of 0.08R, and for a total length of 0.048R. As shown, there are two transitions from iced to clean surface, and the length is 0.008R. These nine iced rotors are labeled from A to I. Note that the sectional ice thickness is very small compared to the chord, with a maximum thickness of only 0.015c. In the calculations, the advance ratio was set to be 0.2, and the blade-tip speed was 130 m/s. The rotors were operated at a fixed collective pitch of 10 degrees with a same periodic pitch (θ_{1c} =7°, θ_{1s} =-4°).

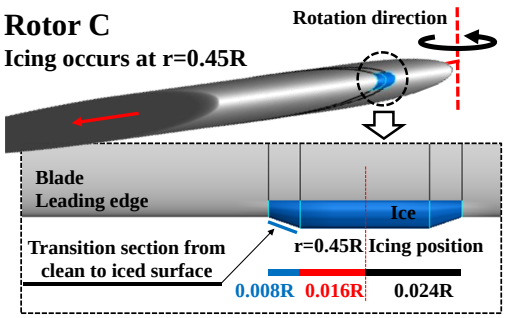

Rotor number	A	B	C	D	E	F	G	H	I
Icing position	0.29R	0.37R	0.45R	0.53R	0.61R	0.69R	0.77R	0.85R	0.93R

(a) Icing position on rotors

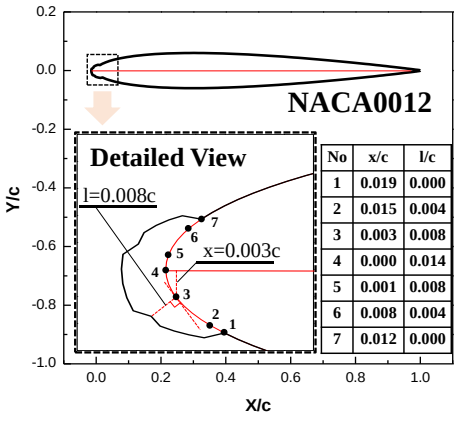

No	x/c	l/c
1	0.019	0.000
2	0.015	0.004
3	0.003	0.008
4	0.000	0.014
5	0.001	0.008
6	0.008	0.004
7	0.012	0.000

(b) The detail view of the ice shape

Figure 24. Iced rotors with different icing positions.

Figure 25 shows the lift coefficients of the iced rotors next to the clean. As can be seen, the change in rotor lift mainly occurs on the advancing blade, from 30° to 90° azimuth. Dynamic stall may occur since the angle is large on the retreating blade, and the influence of ice accretion on lift coefficient is less significant compared with that on the advancing blade. In the figure 25(b), the displayed zone of the lift coefficient from 25° to 65° azimuth is enlarged. As seen, there is no obvious change in the lift coefficient between rotors A (icing at 0.29R) and I (icing at 0.93R), and the drop of the lift coefficient of rotor F (icing at 0.69R) is the largest, up to 3.41% at 60° azimuth. In figure 25(c), the differences of the lift coefficient due to ice at two azimuth angles (30° and 60° azimuth) are given. Due to the effect of ice accretion, the reduction of the lift coefficient increases along the spanwise direction from blade root till 0.7R blade section, and then decreases. So, a small ice shape has almost no effect on the lift coefficient of rotors when the icing position is near the blade tip or the blade root. When the icing position is near the middle of blade, the lift coefficient obviously decreases.

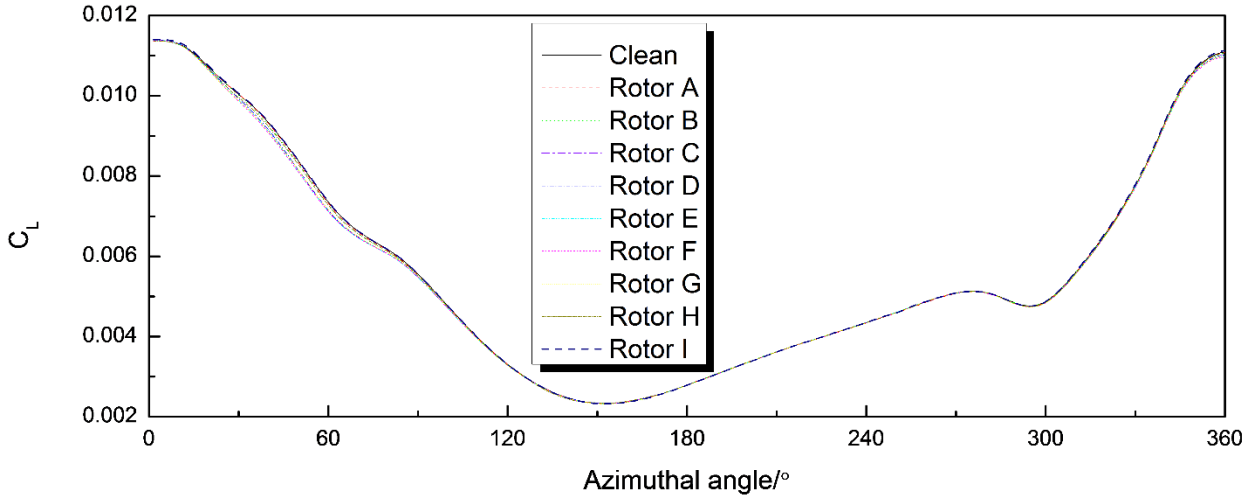

(a) Lift coefficient

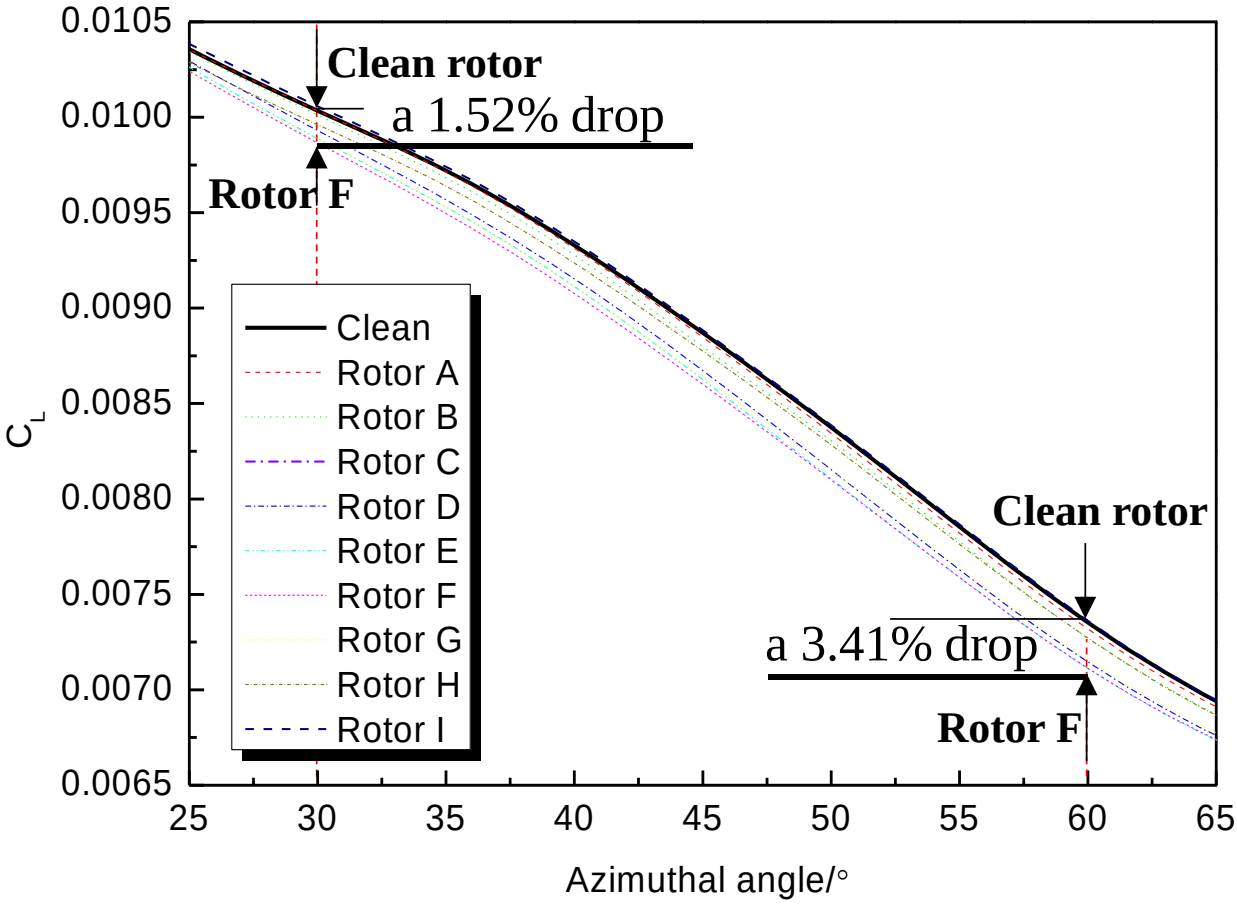

(b) Local enlarged image

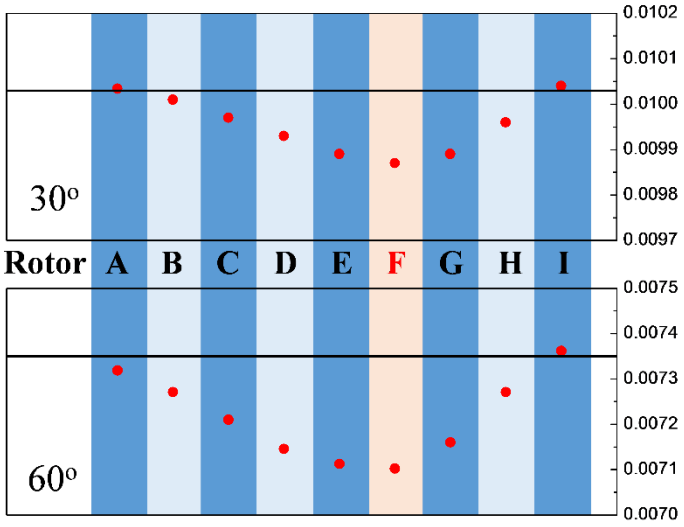

(c) Lift coefficient at 30° and 60° of azimuth

Figure 25. Comparisons of rotor lift coefficient of iced and clean rotors.

Figure 26 shows torque coefficients of different iced rotors alongside the clean. Overall, the torque coefficients of iced rotors all increase compared with the clean rotor, although the average torque coefficient does not change

significantly. The change in rotor torque mainly occurs in a narrow range from -30° to 30° blade azimuth. In figure 26(b), the displayed zones of the lift coefficient from 0° to 60° azimuth and from 300° to 360° azimuth are enlarged. As seen, the rotor torque is much influenced by ice when the icing position is near 0.7R, similar to the variation of the lift coefficient. At 20° azimuth, the increase of the torque coefficient for rotor F was the largest, followed by rotors G and E. At 360° azimuth angle, the increase of the torque coefficient for rotor G is the largest, followed by rotors F and H. As a result, the influence of the small ice on aerodynamic characteristic of rotor should not be neglected when the icing position is near the 0.7R blade section, and deicing near the 0.7R section of the blade may be preferred at the beginning of ice accretion on rotors.

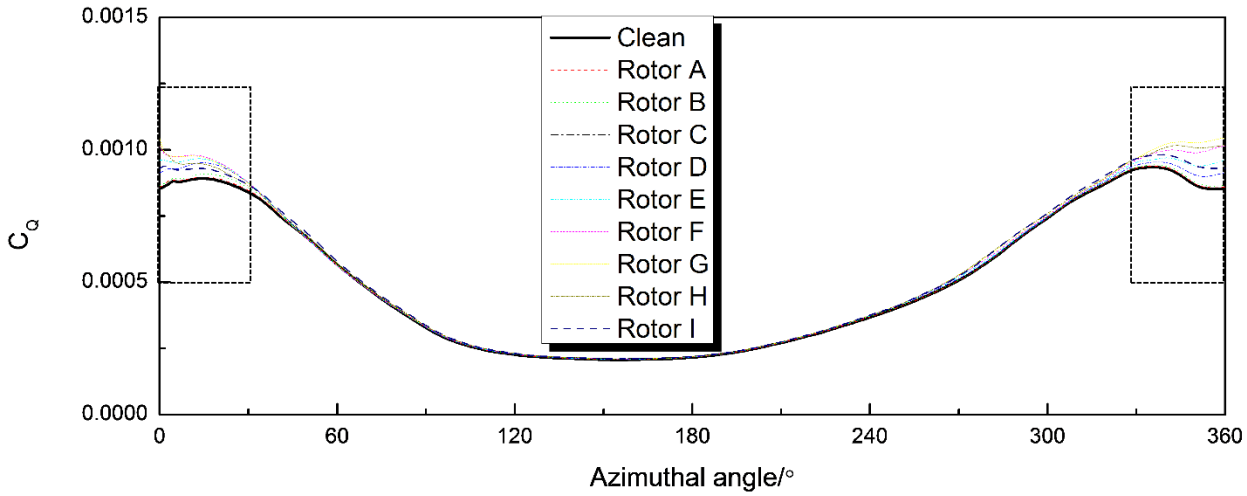

(a) Torque coefficient

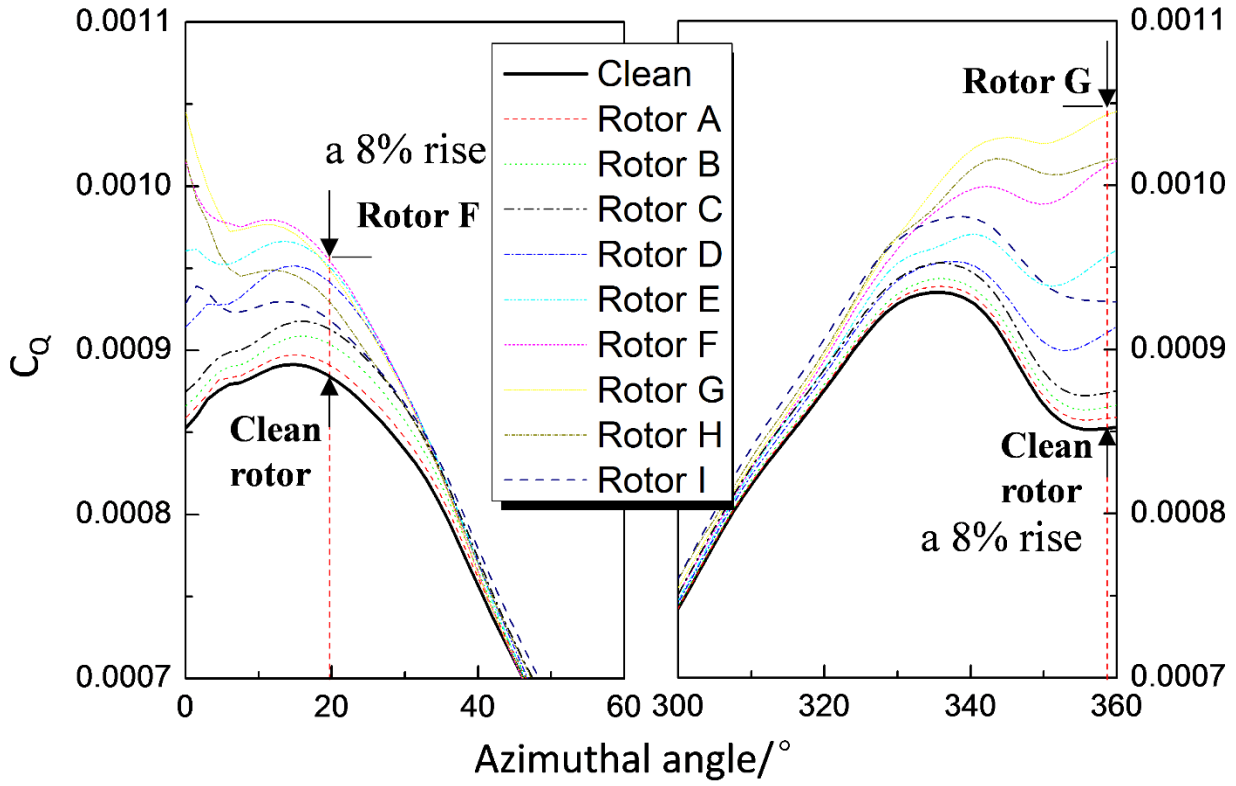

(b) Local enlarged image

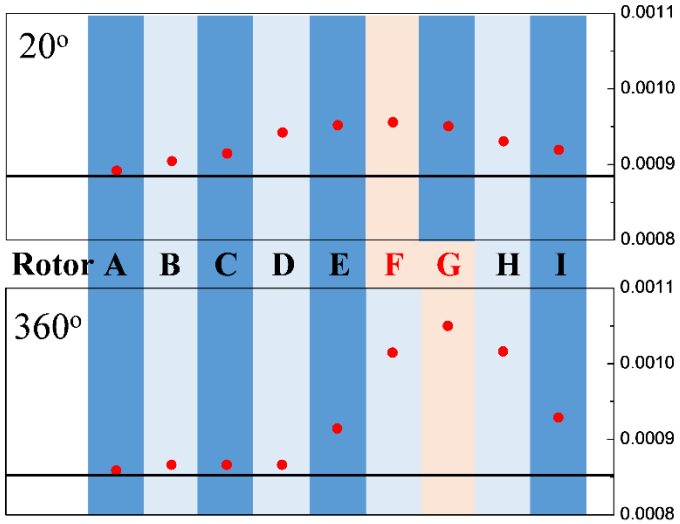

(c) Torque coefficient at 30° and 60° of azimuth

Figure 26. Comparisons of rotor torque coefficient of iced and clean rotors.

To reveal the influence of the icing position on the aerodynamic characteristics of the rotor in forward flight, the pressure distributions on the blade surface of three iced rotors at 60° azimuth are given in Figure 27. Since the ice amount is very small, there is no obvious change in the pressure distributions on the lower surface, as seen in the Figure 28. On the upper surface, the small ice amount does not only affect the pressure distribution near the icing

position, but it also changes the pressure in a larger area on the blade surface. When the icing position is 0.69R (rotor F), the change of the pressure distribution from 0.69R to 0.93R is visible. Since the rotor lift is mainly supplied from that blade area, the lift is worst affected when icing occurs near 0.69R for this condition.

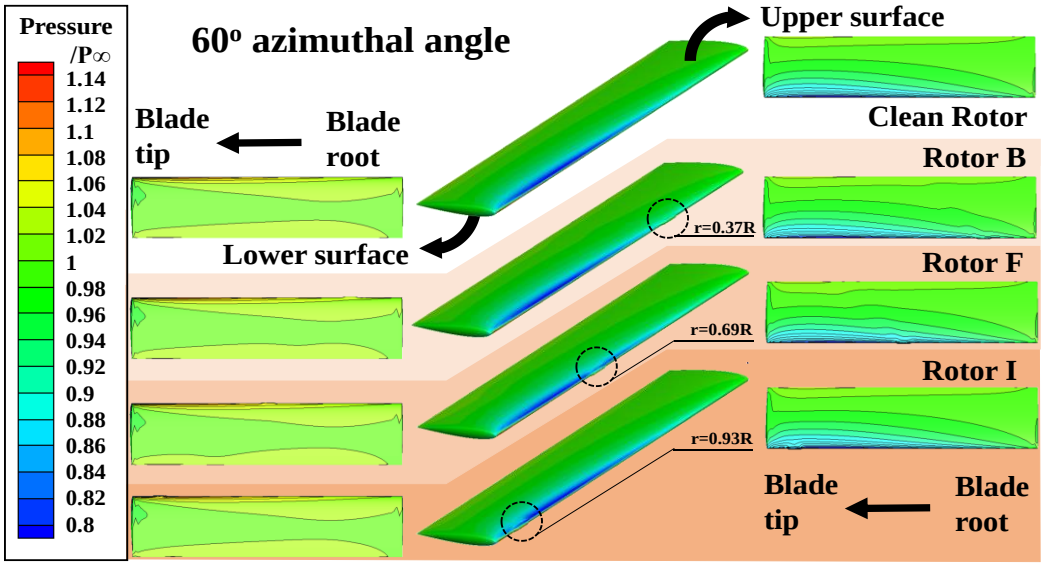

Figure 27. Pressure distributions on the blade surface at 60° azimuth angle.

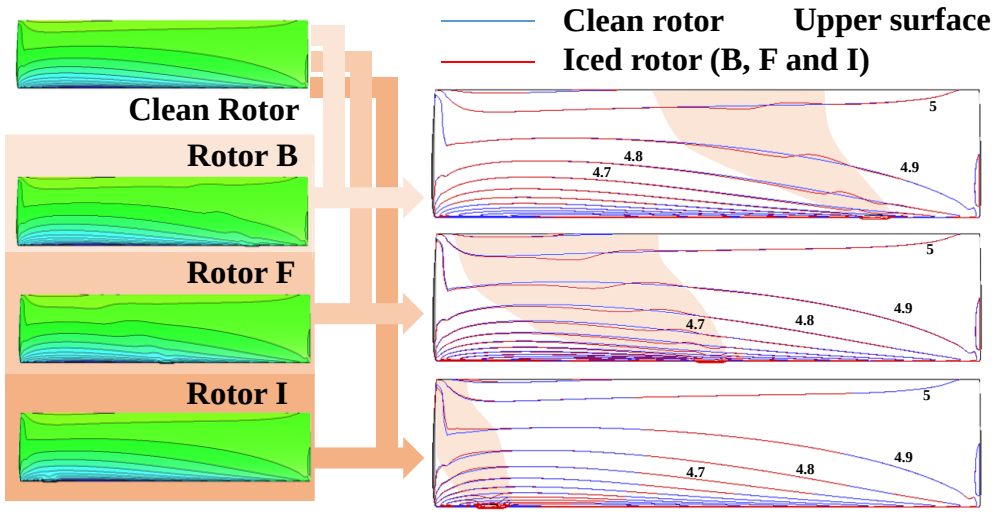

Figure 28. Comparison of pressure distributions between clean and iced rotors at 60° azimuth angle.

The comparison of the pressure distributions of the blade sections between rotor F and the clean one is given in Figure 29. At r=0.69R, there is an additional, small ice shape compared with the clean rotor, and the pressure distribution changes, especially near the leading edge of the blade. At r=0.65R, the shape of blade section of rotor F is the same as the clean rotor, and the pressure distribution changes slightly. At r=0.73R, although the shapes are the same, the difference of the pressure distribution is visible, and it is bigger even than that of the icing position (0.69R).

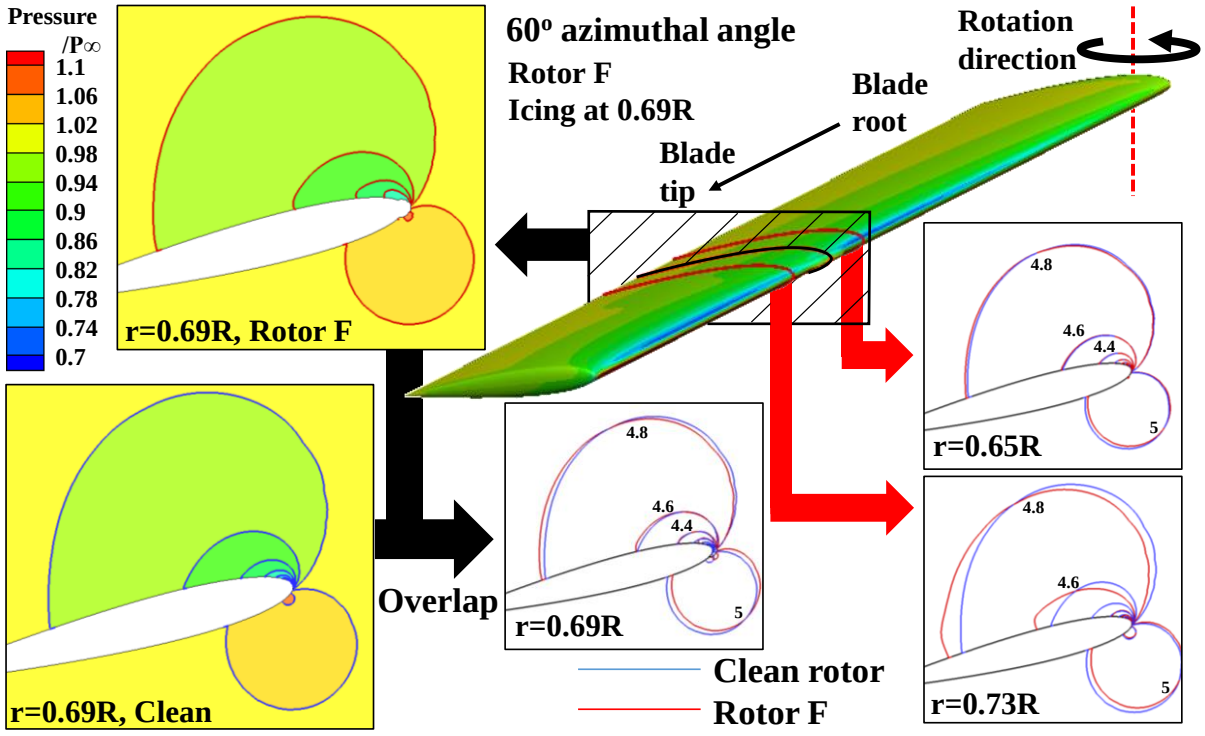

Figure 29. Comparisons of rotor lift coefficient of iced and clean rotors.

CONCLUSIONS

Based on the numerical simulation of rotor icing, the influence of the ice accretion on the aerodynamic characteristics of a rotor in forward flight is calculated and analyzed. The main conclusions are:

1) In forward flight, the influence of the ice accretion on the blade lift coefficient is larger on the advancing blade than the retreating. Normally, there is an obvious increase in the torque coefficient when ice forms on the blade surface. However, at the beginning of the ice accretion, the increase of the torque coefficient is very small. This could lead to a late activation of the deicer, and late removal of the ice.

2) In a blade section of an iced rotor, the pressure coefficient often has a decrease on the lower surface and an increase on the upper, resulting in loss of lift. Since the chord is longer by the accreted ice at the leading edge of the blade, the sectional lift force may increase for some cases. Overall, the influence of the ice accretion on the sectional aerodynamic characteristics gradually increases along the blade radius.

3) At higher temperatures, the pressure on the lower surface markedly decreases, and it is smaller than the pressure on the upper surface in some areas, result in a negative lift force. This phenomenon is more obvious near the blade

tip, and is the main reason for the reduction of the lift force. At lower temperatures, although the pressure on the lower surface decreases, the area of the negative lift zone is smaller compared with that at higher temperatures.

4) If the icing position is close to the blade tip or root, a small amount of ice has no effects on the aerodynamic characteristics of the rotor. If the icing position is closer to the 0.7R blade section, the influence on aerodynamics is larger. As a result, deicing near the 0.7R blade section may be preferred at the beginning of the ice accretion on the whole blade.

ACKNOWLEDGEMENTS

This study was co-supported by the National Natural Science Foundation of China (Nos. 11272150 and 11572156).

REFERENCES

[1] Lynch, F. T., and Khodadoust, A., "Effects of ice accretions on aircraft aerodynamics," Progress in Aerospace Sciences, Vol. 37, No.8, 2001, pp. 669-767. DOI: 10.1016/S0376-0421(01)00018-5

[2] Flemming, R., and David, A., "High Speed Ice Accretion on Rotorcraft Airfoils," NASA/CR 3910, 1985.

[3] Hartman, P., Narducci, R., Peterson, A., Dadone, L., Mingione, G., Zanazzi, G., and Brandi, V., "Prediction of Ice Accumulation and Airfoil Performance Degradation: A Boeing-CIRA Research Collaboration," AHS International 62th Annual Forum, Phoenix, Arizona, May 9-11, 2006.

[4] Korkan, K. D., Cross, E. J., and Miller, T. L., "Performance Degradation of a Model Helicopter Rotor with a Generic Ice Shape," Journal of Aircraft, Vol. 21, No. 10, 1984, pp. 823-830. DOI: 10.2514/3.45049

[5] Korkan, K. D., Dadone, L., and Shaw, J. R., "Performance Degradation of Helicopter Rotor in Forward Flight due to Ice," Journal of Aircraft, Vol. 22, No. 8, 1985, pp. 713-718. DOI: 10.2514/3.45191

[6] Lee, J., "Aerodynamic Evaluation of a Helicopter Rotor Blade with Ice Accretion in Hover," AIAA paper 1984-0608, 1984.

[7] John, D. L., "Documentation of Ice Shapes on the Main Rotor of a UH-1H Helicopter in Hover," NASA 168332, 1984.

[8] Wright, W., “Further Refinement of the LEWICE SLD Model,” AIAA paper 2006-0464, 2006.

[9] Hedde, T., and Guffond, D., “ONERA Three-dimensional Icing Model,” AIAA Journal, Vol. 33(6), 1995, pp. 1038-1044.

[10] Gori, G., Zocca, M., Garabelli, A., Guardone, A., and Quaranta, G., “PoliMice: A simulation framework for three-dimensional ice accretion,” Applied Mathematics and Computation, Vol. 267, 15 September 2015, pp. 96-107. DOI: 10.1016/j.amc.2015.05.081

[11] Tran, P., Brahimi, M. T., Paraschivoiu, I., Pueyo, A., and Tezok, F., “Ice Accretion on Aircraft Wings with Thermodynamic Effects,” Journal of Aircraft, Vol. 32, No. 2, 1995, pp. 444-446. DOI: 10.2514/3.46737

[12] Fortin, G., Laforte, J., and Ilinca, A., “Heat and Mass Transfer during Ice Accretion on Aircraft Wings with an Improved Roughness Model,” International Journal of Thermal Sciences, Vol. 45, No. 6, 2006, pp.595-606. DOI: 10.1016/j.ijthermalsci.2005.07.006

[13] Srinivasan, G. R., Baeder, J. D., Obayashi, S., and Mccroskey, W. J., “Flowfield of a Lifting Rotor in Hover - A Navier-Stokes Simulation,” AIAA Journal, Vol. 30, No. 10, 1992, pp. 2371-2378. DOI: 10.2514/3.11236

[14] Rajagopalan, R. G., Mathur, S. R., “Three Dimensional Analysis of a Rotor in Forward Flight,” Journal of the American Helicopter Society, Vol. 38, No. 3, 1993, pp. 14-25. DOI: 10.2514/6.1989-1815

[15] Narducci, R., and Kreeger, R. E., “Analysis of a Hovering Rotor in Icing Conditions,” NASA TM-217126, 2012.

[16] Narducci, R., Orr, S., and Kreeger, R. E., “Application of a High-Fidelity Icing Analysis Method to a Model-Scale Rotor in Forward Flight”, NASA TM-217122, 2012.

[17] Rajmohan, N., Bain, J., Nucci, M., and Kreeger, R., “Icing Studies for the UH-60A Rotor in Forward Flight,” Proceedings of the 2010 AHS Aeromechanics Specialists’ Conference, American Helicopter Society, San Francisco, CA, Jan 20-22, 2010, pp. 261-276.

[18] Bain, J., Cajigas, J., Sankar, L., Flemming, R. J., and Aubert, R., “Prediction of Rotor Blade Ice Shedding

Using Empirical Methods," AIAA paper 2010-7985, 2010.

[19] Zhao, G. Q., Zhao, Q. J., and Chen, X., "New3-D Ice Accretion Method of Hovering Rotor Including Effects of Centrifugal Force," Aerospace Science and Technology, Vol. 48, Jan. 2016, pp. 122-130. DOI: 10.1016/j.ast.2015.10.018

[20] Wang, Z., and Zhu, C., "Study of the Effect of Centrifugal Force on Rotor Blade Icing Process," International Journal of Aerospace Engineering, Vol. 2017, Article ID 8695170, 9 pages, 2017. DOI:10.1155/2017/8695170.

[21] Wang, Z., Zhao, N., and Zhu, C., "Numerical Simulation for Three-dimensional Rotor Icing in Forward Flight," Advances in Mechanical Engineering, Vol. 10, No.4, 2018. DOI: 10.1177/1687814018772404

[22] Kelly, D., Habashi, W. G., Quaranta, G., Masarati, P., and Fossati, M., "Ice Accretion Effects on Helicopter Rotor Performance, via Multibody and CFD Approaches," Journal of Aircraft. Vol. 55, No. 3, 2018, pp. 1165-1176. DOI: 10.2514/1.C033962

[23] Chen, X., and Zhao, Q. J., "Numerical Simulations for Ice Accretion on Rotors Using New Three-Dimensional Icing Model," Journal of Aircraft, Vol. 54, No. 4, 2017, pp. 1428-1442. DOI: 10.2514/1.C033986

[24] Zhao, Q. J., Zhao, G. Q., Wang, B., Wang, Q., Shi, Y. J., Xu, G. H., "Robust Navier-Stokes Method for Predicting Unsteady Flowfield and Aerodynamic Characteristics of Helicopter Rotor," Chinese Journal of Aeronautics, Vol. 31, No. 2, 2018, pp. 214-224. DOI: 10.1016/j.cja.2017.10.005

[25] Papadakis, M., Hung, K. E., Vu, G. T., "Experimental Investigation of Water Droplet Impingement on Airfoils, Finite Wings, and an S-Duct Engine Inlet," NASA.TM-2002-211700

[26] Wright, W. B., and Rutkowski, A., "Validation Results for LEWICE 2.0," NASA/CR-208690, 1999.

[27] Marques, S., Badcock, K. J., Gooden, J. H. M., Gates, S., and Maybury, W., "Validation Study for Prediction of Iced Aerofoil Aerodynamics," The Aeronautical Journal, Vol. 114, No.1152, 2010, pp.103-111. DOI: 10.1017/S0001924000003572

[28] Lee, J. D., "Documentation of Ice Shapes on the Main Rotor of a UH-1H Helicopter in Hover," NASA 168332,

1984.

[29] Fortin, G., and Perron, J., “Spinning Rotor Blade Tests in Icing Wind Tunnel,” AIAA paper 2009-4260, 2009.

[30] Tong, X. L., and Luke, E. A., “Eulerian Simulations of Icing Collection Efficiency using a Singularity Diffusion Model,” AIAA paper 2005-1246, 2005.

[31] Miller, T. L., and Bond, T. H., “Icing Research Tunnel Test of a Model Helicopter Rotor,” NASA/TM-101978, 1989.

[32] Kong, W., and Liu, H., “Development and Theoretical Analysis of an Aircraft Supercooled Icing Model,” Journal of Aircraft, Vol. 51, No.3, 2014, pp. 975-986. DOI: 10.2514/1.C032450

[33] Kim, J. W., Park, S. H., and Yu, Y. H., “Euler and Navier-Stokes simulations of helicopter rotor blade in forward flight using an overlapped grid solver,” AIAA Paper, 2009-4268, 2009.